

Flux driven turbulence on open field lines

Y. Sarazin¹, Ph. Ghendrih¹, X. Garbet¹, V. Grandgirard¹
S. Benkadda², P. Beyer²

September 7, 2001

¹ *Association EURATOM-CEA, CEA Cadarache, 13108 St-Paul-Lez-Durance, France*

² *Equipe Dynamique des Systèmes Complexes, Laboratoire PIIM CNRS - Université de Provence, 13397 Marseille, France*

Turbulence in the scrape-off layer (SOL) is investigated using a 2D fluid model for interchange instability. A constant driving flux governs the dynamics of both equilibrium and fluctuating parts of density and electric potential. The turbulent flux exhibits intermittent bursts, called avalanches. These events account for a significant part of the total transport, and lead to non-gaussian probability density functions. The time average density profile looks exponential, and the SOL width increases weakly with the driving source (scaling exponent $2/9$). The dynamics of zonal flows is found to strongly depend on viscosity ν . The lower ν , the larger the magnitude of the velocity shear fluctuations. Ultimately, a large shearing significantly reduces the correlation length of the fluctuations, and hence the transport. Finally, the impact on turbulence of a local biasing is investigated, possibly modeling Langmuir probe measurements. A negative biasing, leading to the extraction of up to 75% of the ion saturation current, is found to strongly modify the dynamics of the transport, even outside the exact location of the biasing. At the probe, the time averaged density decreases by a factor 4, and the large amplitude low frequency fluctuations of the density field — strong avalanches — are suppressed. The electric potential fluctuations exhibit essentially a shift toward larger frequencies. These results put forward the possible strong departure between Langmuir probe turbulence measurements and the "real" ambient turbulence, as well as possible mismatch in the measurement of the ion saturation current.

1 Introduction

As for core plasma, it is well known that turbulent transport plays an important role in the plasma Scrape-Off Layer since it governs the cross-field transport. It is interesting to note, in particular, that the SOL width is generally understood as characterizing the balance between parallel transport and cross-field transport. As a consequence, the SOL width is such that it is equally distant from the Last Closed Magnetic Surface via cross-field transport as to the wall via parallel transport. From this picture, cross-field transport is dominant within the first e-folding length of the SOL. Although this region of the plasma is particularly suited to investigate SOL turbulence with probe measurements [1], there is still a significant gap to fill in order to bridge the SOL modeling to the turbulence measurements [2]. In fact, the problem of cross-field transport also interferes with the Langmuir probe measurements themselves [3]. Last but not least, the SOL width governed by the cross-field transport plays a crucial role in the design of next step devices due to the very large power handled in these devices. As such, accurate values and an extrapolation law are badly needed. Unfortunately the attempts in that direction have not been successful. More worrying, recent data seem to indicate the existence of still narrower SOL width [4]. The need for theoretical investigation is clearly needed to step ahead in this complex problem.

A significant change in the analysis of plasma turbulence has taken place as the drive of the system was considered to be a flux rather than a gradient. Indeed, the standard analysis of systems out of thermodynamical equilibrium aims at determining the flux resulting from an imposed gradient. The latter characterizes the "distance" from the thermodynamical equilibrium. Let us consider the density field and hence the relationship between the particle flux and density. In all fusion plasmas, the system is driven away from equilibrium by the particle injection rate and particle recycling. As such, our systems are flux driven rather than gradient driven. This change in driving force leads to significant modifications in the dynamics of the turbulent response, with continuous reorganisation of the turbulent eddies and locally, repeated evolution from the linear stage to the nonlinear saturation of the turbulence. In addition to this change in approach, the interest in the flows self generated by the turbulence has increased [5] since these flows, namely the Zonal Flows, seem to play a major role in the non-linear saturation of turbulence [6]. As a result of these two inputs, turbulent models exhibit intermittent behaviour with avalanche-like propagation – related to front propagation [7] and/or streamers [8] – and a large variety of dynamics, as predicted theoretically [9]. This behaviour is observed in numerous fluid models for edge and core turbulence [10, 11, 12, 13], and has also been tackled for SOL turbulence [14]. Experimental evidence of large scale transport is also reported [15].

In the present paper, we address issues that are at the crux of present experimental investigation of the SOL. In section 2, we review the status of the 2-D fluid model that is used. The scaling of the SOL width with increasing source term is presented there. In section 3, we address the difficult issue of the interplay of viscosity with the behaviour of avalanche transport. This investigation is most important since one finds that this viscosity seems to control the poloidal flows self-generated by the turbulence. Since these flows are believed to determine the saturation level of the turbulence, one readily understands the importance of this analysis. Finally, in section 4, we model the turbulence response to probe ion saturation measurements.

2 Interchange instability in the SOL

2.1 Flux driven 2D model

Strong density \tilde{n} and electric potential $\tilde{\phi}$ fluctuations are experimentally observed in the SOL of fusion devices, accounting for the heat anomalous transport [16]. Interchange instability is supposed to play a prominent role in this turbulent transport. Indeed, the large sheath resistivity $\sigma_{||}$ destabilises interchange electrostatic modes in the SOL, driven by the pressure gradient in the bad curvature – Low Field Side – region [17, 18]. Following a previous work [14] and supported by experimental observations [19], the model discussed in this paper only considers flute-like modes, hence $k_{||} = 0$. More precisely, for a SOL between two toroidal limiters located at symmetrical poloidal angles $\pm\Delta\theta$, the modes are such that $k_{||} = 2/L_{||} = 1/qR_0\Delta\theta$.

A field line average then makes the problem 2-D. Further assuming a constant electron temperature T_e and cold ions yields two parameters: the normalized sheath conductivity $\sigma_{||} = \rho_s/L_{||}$ and the average field line curvature $g = [(1+s)\sin\Delta\theta - s\Delta\theta\cos\Delta\theta]2q\rho_s/L_{||}$. Both the normalized sheath conductivity and the curvature exhibit a ρ_* dependence through the ratio $\rho_s/L_{||}$. The normalized system is then derived from particle and charge conservation laws:

$$\begin{aligned} d/dt \, n &= \sigma_{||} n \exp(\Lambda - \phi) + D\nabla_{\perp}^2 n + S \\ d/dt \, \nabla_{\perp}^2 \phi &= \sigma_{||} \{1 - \exp(\Lambda - \phi)\} - g \, \partial_y \text{Log}(n) + \nu \nabla_{\perp}^4 \phi \end{aligned} \quad (1)$$

where the total time derivative stands for the Lagrangian derivative $d/dt \doteq \partial_t + [\phi, \cdot]$. n and ϕ are the *total* density and electric potential, and not only their fluctuating parts. In the SOL, the destabilising density gradient is build up by the source term, namely by the ionization of recycling neutrals, and by the particle influx S crossing the separatrix. Only the latter is retained here. Finally, the following normalization is adopted:

$$\begin{aligned} n &\rightarrow n/n_0; & \phi &\rightarrow e\phi/T_e \\ x &= (r - a)/\rho_s; & y &= a\theta/\rho_s; & t &\rightarrow \Omega_s t \\ (D, \nu) &\rightarrow (D, \nu) \rho_s c_s \end{aligned}$$

Here, the Larmor radius is defined by $\rho_s = c_s/\Omega_s$, with $\Omega_s = eB/m_i$ and $c_s = (T_e/m_i)^{1/2}$. The floating potential $\Lambda = \frac{1}{2}\text{Log}(\frac{4}{\pi}m_i/m_e)$ which develops at the end points of the field lines (the sheath), is governed by the difference between electron and ion inertia. In steady state conditions and in the absence of any biasing, it ensures a zero current at the end points of the field lines. Unless specified, typical numerical parameters are $\sigma_{||} = 2.27 \cdot 10^{-4}$, $g = 5.72 \cdot 10^{-4}$, $D = 2 \cdot 10^{-2}$, with $\rho_s \approx 3.4 \cdot 10^{-4}m$, $c_s \approx 9.8 \cdot 10^4 m.s^{-1}$ and $\Omega_s \approx 2.9 \cdot 10^8 s^{-1}$. Box grid is 128×128 , with $2\rho_s$ per grid point. The code is solved using a predictor-corrector method in time, and is pseudo-spectral in both directions [20]. The particle source is constant in time and poloidally (along y), with a gaussian radial shape $S(x) = S_0 \exp[-(x/\lambda_S)^2]$, with $S_0 = 10^{-2}$ and $\lambda_S = L_x/30$. Such a treatment allows one to investigate two separate SOL regions: a stable one, where density gradient and curvature have opposite signs, leading to a SOL width λ_{SOL} governed by collisional transport, and the turbulent region in which curvature and $\partial_x \bar{n}$ are colinear. The latter part is the turbulent SOL investigated in this paper.

2.2 Transport and SOL width

Most of the dynamical properties of the system described by Eq. 1 are discussed in a previous paper [14]. Basically, turbulent transport looks intermittent and bursty, and is dominated by long range transport events which propagate almost ballistically and called avalanches. Such a dynamics is associated with convective cells mainly elongated radially, reminiscent of streamers [8]. The probability density function (PDF) of the equilibrium (*i.e.* poloidally averaged) radial flux at a given location is shown on Fig. 1. It can be described by two distinct components: a gaussian centered on zero – and hence of vanishing flux – and a log-normal distribution, accounting for the distribution tail which extends toward large outbursts. The gaussian shape is expected to model the underlying diffusive-like transport, governed by both small-size turbulent eddies and the collisional transport associated to D . Surprisingly, the most probable equilibrium flux is negative. Such a decomposition of the PDF allows one to quantify the impact of rare but large events on the overall transport. In this case, it turns out that 44% of the total flux is carried out by events whose probability lies outside the 4σ domain. σ refers here to the mean deviation of the gaussian. The intermittent character is also reported experimentally [21, 22]. Exponential tails are predicted theoretically for the local turbulent radial flux, provided density and electric potential fluctuations are gaussian [23]. Such a condition is however not fulfilled in the 2D interchange turbulence studied here. Indeed, local fluctuations \tilde{n} and $\tilde{\phi}$ exhibit non-gaussian PDFs. PDFs of radial and poloidal density gradients are plotted on Fig. 2. The PDF of $\partial_x \bar{n}$ is asymmetric, with an exponential tail extending toward strong unstable gradients. These gradient fronts are well correlated with the avalanche-like transport events responsible for a similar tail on the PDF of the flux. On the contrary, the PDF of the poloidal density gradient looks rather gaussian, suggesting the poloidal transport is diffusive-like.

The time averaged and instantaneous density profiles $\langle \bar{n}(x) \rangle$ and $\bar{n}(x, t_0)$, both recorded in the saturated phase of the non-linear regime, are shown on Fig. 3. The source profile is shown as well. \bar{n} looks rather smooth, and exhibits an exponential decay although turbulent transport is not diffusive-like. Interestingly enough, radial convective transport also leads to an exponential density profile. Should the parallel transport be balanced by convective turbulent transport of effective velocity v_{eff} , then the equilibrium time average density is exponential with an e-folding length of $\lambda_{SOL} = L_{||} v_{eff} / c_s$. In the case presented on Fig. 3, the SOL e-folding length is of the order of $\lambda_{SOL} \approx 45 \rho_s$ in the turbulent region, about 10 times larger than the one in the stable SOL, on the left handside of the source. Turbulent activity can also lead transiently to very steep gradients, as exemplified on Fig. 3. Gradient lengths equal to the one generated by collisional transport develop locally. These gradient fronts are associated to avalanche-like events.

An important issue for fusion deals with the scaling of λ_{SOL} with the driving flux $\Gamma_0 \doteq \int_0^{L_x} S(x) dx$. Indeed, present day technical limitations of fusion devices include the limited capability of plasma facing components to extract a large amount of power. In that respect, spreading the outward power flux over a large region is highly beneficial. As such, the turbulent SOL a factor 10 times larger than the classical SOL allows to reduce the energy flux by a factor 10. Figure 4 shows how the SOL width λ_{SOL} increases with Γ_0 , all other parameters remaining unchanged. These numerical results have been obtained with the following set of normalized parameters: $g = 5.10^{-4}$, $\sigma_{||} = 10^{-5}$, $D = \nu = 5.10^{-4}$, and a grid size equal to 64×64 . The favourable point is the increase of λ_{SOL} with Γ_0 , which is thus potentially able to slightly reduce the thermic constraints on plasma

facing materials. However, this increase remains weak: λ_{SOL} only increases by a factor of about 2 when S is multiplied by 80. Assuming a power law dependence would lead to $\lambda_{SOL} \sim S^{2/9}$. Such a result puts forward the crucial interest in alternative means of controlling the SOL width λ_{SOL} .

3 Impact of viscosity on the dynamics of turbulence

3.1 Viscosity, Zonal Flows and transport

Recently, turbulent diffusivity χ_i has been observed to increase with normalized collision frequency ν^* in gyrokinetic (GK) numerical simulations of ion temperature gradient (ITG) turbulence [24]. This result looks surprising because it contradicts linear predictions. Indeed, for linear instabilities of the Rayleigh-Bénard type, like interchange or ITG, the Reynolds number \mathcal{R} measures the departure from linear marginal stability. \mathcal{R} is inversely proportionnal to the viscosity ν . Hence, lowest viscosity cases are linearly the most unstable since they have the largest \mathcal{R} , and should be therefore "*the most turbulent*" ones with the largest transport. On the contrary, the observed increase of χ_i with ν^* appears in the nonlinear regime as a consequence of the linear damping of Zonal Flows (ZF) by viscosity. The reason is the following. Numerous studies, both theoretical [25, 26], numerical [6, 12] and experimental [27, 28] point out the role of ZF in the regulation of turbulence and, in fine, in the magnitude and dynamics of turbulent transport. The advocated mechanism for this self-regulation of turbulence relies on the shearing of convective cells by the self-generated mean poloidal velocity \bar{v}_y , the so-called ZF. Efficient ZF shearing tends to reduce the radial correlation of convective cells, hence lowering the transport [29]. Numerical GK simulations show indeed a strong increase in the radial size of convective cells and in transport when such ZF are artificially suppressed [6]. Hence, ZF magnitude is of crucial importance in determining the turbulent transport level. An important point is that ZF are damped by collisions and viscosity. Especially, in the collisionless regime, ZF are expected theoretically to remain undamped and stable with respect to secondary instabilities close to the instability threshold [30, 31]. A striking consequence is the ability of self-generated sheared flows to completely suppress any turbulent transport in GK simulations of ITG modes run just above the marginal linear stability [32].

As far as SOL transport is concerned, an important issue already mentionned deals with the capability of fusion devices to increase λ_{SOL} in view of spreading the outward power flux onto the target plates. Theoretically, viscosity emerges from the anisotropy of the pressure tensor. In fluid codes, the viscosity coefficient ν appears as an *ad hoc* parameter. It is essential since it ensures the damping of small scale structures. However, it is usually considered that this term has no impact on the code outputs since, generally, the turbulence generates a much larger diffusivity or viscosity. In the framework of self-regulation of turbulence by ZF, the viscosity appears, however, to be a key parameter [33]. Simulations presented in section 3.2 confirm that it governs the ZF, and hence the radial extent of the avalanches.

In the system described by Eq. 1, ZF are driven by the Reynolds stress, which dominates by about one order of magnitude over the sheath term. Linear damping of the mean poloidal velocity \bar{v}_y is then ensured by the viscosity. \bar{v}_y satisfies the following equation:

$$\partial_t \bar{v}_y = -\partial_x \overline{\tilde{v}_x \tilde{v}_y} - \sigma_{||} \int_0^x \overline{\Lambda - \phi} dx + \nu \partial_{xx} \bar{v}_y$$

The following section investigates the effect of the normalised viscosity ν on both turbulence dynamics and transport magnitude, which governs the SOL e-folding length λ_{SOL} . Special attention is paid to the role of ZF in this regulation.

3.2 Dynamics of Zonal Flows

Two simulations with different values of ν have been performed: $\nu_0 = 5.10^{-3}$ and $\nu_1 = 2.10^{-2}$. The linear properties of these two runs are summarized on Fig. 5. The maximum growth rate for ν_0 , equal to $\gamma_{0max} \approx 11.10^{-3}$, is about 1.4 times larger than for ν_1 . Linear damping at small scales is proportionnal to $\min(D, \nu) k_{\perp}^2$. This explains why smaller scales become linearly unstable for smaller values of ν . Quantitatively, linear stability analysis suggests that structures roughly 1.5 times smaller are expected to develop in both directions (x and y) for low viscosity (ν_0 case) when compared to large viscosity (ν_1 case). However, the lower k_y cut-off wave vector is independent of ν , as seen on Fig. 5b. Indeed, large scales are damped by the sheath conductivity σ_{\parallel} . Note also that $k_x = 0$ modes are the most linearly unstable modes in both cases, whatever k_y . As a consequence, linear properties do not allow to predict any finite radial length of turbulence. This result is no longer true when accounting for non monotonuous radial profile of the equilibrium poloidal velocity \bar{v} . In this case, the second radial derivative of \bar{v} is damping large scale fluctuations, leading to $\gamma = -\sigma_{\parallel} - \frac{k_y^2}{4\sigma_{\parallel}k_{\perp}^2} \bar{v}''^2$ when $k_{\perp} \rightarrow 0$.

As shown on Fig. 6, \bar{v}'' appears to introduce a linear characteristic radial scale of the fluctuations. Indeed large radial scales are linearly stable for strong enough \bar{v}'' . Also, the linear growth rate depends neither on \bar{v} , which only introduces a Doppler shift, nor on the velocity shear \bar{v}' , whose linear system does not depend on. As a result, the break-up of convective cells along the radial direction by an equilibrium or time dependent (*i.e.* ZF) velocity shear is fundamentally a nonlinear process in the interchange turbulence.

Figures 7-8 show the complex dynamics of ZF in these two runs. First of all, the radial dynamics of ZF in the lower ν case exhibits smaller scales than that of ν_1 . Quantitatively, the k_x Fourier spectrum peaks roughly at the same wave vector in both cases ($k_x \approx 0.2$), but is about 1.4 larger for ν_0 , extending toward larger k_x . In this case, a larger shearing $ik_x \bar{v}_y$ of turbulence eddies is then expected. Secondly, the typical frequency of case ν_0 looks larger than that of case ν_1 . Consistently, the frequency Fourier spectrum is broader for ν_0 by a factor of 2, except in the low density region in the far SOL ($x > 150$), where the ratio is of order of one. Finally, Fig. 9 shows the root mean square of the fluctuations of the shear flow, defined as $\bar{v}'_{rms} \doteq \langle (\partial_x \bar{v})^2 \rangle^{1/2}$. Clearly, \bar{v}'_{rms} is larger in the lowest viscosity case, *i.e.* for ν_0 . This result is in agreement with the linear damping of ZF by the viscosity.

An efficient way to quantify the difference between both simulations is also to measure how they diverge when some random noise is added at a given time to either of the turbulent fields. To test this idea, white noise (WN) has been added to the potential ϕ at time t_0 in both ν_0 and ν_1 cases. The simulations are then restarted, and the quantity $\langle (\tilde{\phi}_{WN} - \tilde{\phi})^2 \rangle^{1/2} / \langle \tilde{\phi}_{WN}^2 + \tilde{\phi}^2 \rangle^{1/2}$ (here, $\langle \dots \rangle$ refers to $\iint \dots dx dy$) is recorded at each time. The result is plotted on Fig. 10. Interestingly, the departure looks roughly exponential in both cases in the initial phase, before reaching a saturation level where the dynamics are totally uncorrelated (fluctuations remain however of the same order of magnitude, as emphasized by the saturation value equal to unity). The normalized exponents at which simulations diverge, analogous to Lyapunov exponents, are equal to $\gamma_0 \approx 2.10^{-3}$ ($\Omega_s t_0 \approx 500$) and $\gamma_1 \approx 5.10^{-4}$ ($\Omega_s t_1 \approx 2000$), respectively for $\nu_0 = 5.10^{-3}$ and $\nu_1 = 2.10^{-2}$. This difference emphasizes the faster dynamics of turbulence at lower value of the viscosity.

This result agrees with the larger shearing at low viscosity, which is expected to decorrelate more efficiently the radial structures. Furthermore, one recovers the expected increase of turbulence as viscosity is decreased (Reynolds number).

3.3 Impact on the transport

Ultimately, the impact of ZF and \bar{v}'_{rms} on turbulent transport is the crucial point. As already mentioned, \bar{v}'_{rms} is expected to reduce turbulent transport by shearing the radial turbulent cells. As a preliminar analysis, the correlation length λ_{correl} is computed at each time in both cases. This characteristic length is derived from the normalized 2D self-correlation function of the electric potential fluctuations, defined as $C_{\tilde{\phi}}(\Delta x, \Delta y, t) \doteq \langle \tilde{\phi}(x, y, t) \cdot \tilde{\phi}(x + \Delta x, y + \Delta y, t) \rangle_{x,y} / \langle \tilde{\phi}(x, y, t)^2 \rangle_{x,y}$. Figure 11 exemplifies the way the measurement is performed. The points equal to $\frac{1}{2}$ form an ellipse centered on $(\Delta x, \Delta y) = (0, 0)$, whose largest diameter defines λ_{correl} . λ_{correl} points essentially in the radial direction. λ_{\perp} corresponds to the width of the ellipse in a direction transverse to λ_{correl} .

It turns out that the smaller the viscosity, the larger the shearing flow, and the smaller the correlation length, as exemplified on Fig. 12. In the ν_1 case, λ_{correl} exhibits very large transient excursions, almost covering the entire size of the system along the radial direction. These transient excursions appear sometimes as a percolation mechanism between radial cells separated by defects. Such structures look very reminiscent of streamers, *i.e.* of convective cells characterized by $k_x \approx 0$. Accordingly, the largest avalanches are observed in this simulation, where density fronts extend up to the very far SOL, namely $x \equiv (r - a)/\rho_s > 100$. On average, λ_{correl} is 1.4 times larger for ν_1 than for ν_0 . Also, turbulence tends to become more isotropic at small values of the viscosity, since the aspect ratio of turbulence eddies $\lambda_{correl}/\lambda_{\perp}$ decreases with ν (from about 3.2 at ν_1 to 2.3 at ν_0). Consistently with the increase of λ_{correl} with ν , turbulent transport is also increased. The turbulent diffusivity, defined as $D_{eff} = -\langle \bar{\Gamma} \rangle / \langle \partial_x \bar{n} \rangle$, is larger by a factor of about 1.7 in the largest ν case, Fig. 13. A statistical analysis is carried out to quantify the correlation between the dynamics of \bar{v}'_{rms} and transport suppression. As a result, density profile extends farther into the SOL with increasing ν , leading to a larger SOL width, λ_{SOL} .

4 Modification of the SOL bursty transport by probe measurements

4.1 Current flow pattern due to the turbulent activity

At low β , electrostatic turbulence dominates the transport process. The development of a fluctuating electric potential then governs the cross-field transport in the plasma boundary. The general mechanism to generate such electric fields is the charge separation driven by the curvature drift. As a consequence, damping of the turbulent activity is readily associated to electric currents that inhibit charge separation via parallel electron transport. The sheath resistivity thus plays an essential role in lowering the electric current and therefore providing optimum conditions for turbulence onset.

In the present 2D fluid model, the cross-field electric currents is balanced by loss terms that account for parallel transport through the sheath. The flute assumption imposes

constant values along the field lines, in particular that of the electric potential ϕ . The current loss term at the end plates, j_{\parallel} , is therefore :

$$j_{\parallel} = n(1 - \exp(\Lambda - \phi)) \quad (2)$$

The parameter Λ is the standard sheath potential drop. Vanishing values of j_{\parallel} imposes that $\phi \sim \Lambda$. However, as the electric potential fluctuates close to this mean value, electric currents are driven inwards or outwards at the end points of the field lines depending on the sign of $\Lambda - \phi$. The dependence on n defines the magnitude of the current and stands for the saturation current j_{sat} . (The sound speed does not appear given the normalizations of the density field in this constant temperature model). It is interesting to note that when considering the quasilinear value of the parallel current loss, one finds $\tilde{n}\tilde{\phi}$ while a $\pi/2$ phase shift is found for the radial particle flux, typically $ik_y\tilde{n}\tilde{\phi}$. As a consequence, if the phase shift between the fluctuating density and electric potential maximises the radial transport, it will minimise the parallel electric current. This quasilinear behaviour is still observed in the non-linear regime of the simulations, Fig. 14, where the particle radial flux nv_{Ex} (v_{Ex} being the radial component of the electric drift velocity) and the parallel current $n(1 - \exp(\Lambda - \phi))$ are nearly quadratic in phase, the extremum of one occurring at zeros of the other.

The strong correlation between the cross-field radial transport and the parallel electric current loss at the end points of the field lines readily suggests that an external control of parallel electric current might in turn modify the cross-field transport. The means to control the parallel current is to bias the area of interest. A change of the wall electric potential everywhere will have no effect so that one can readily expect that the biasing geometry must exhibit scales that are comparable to the turbulence scales to have any impact. A typical case of such a biasing is met with probes [34, 35]. On the basis of similar ideas, biasing of probes have been used to control the turbulent activity [36] or for larger probes to trigger edge transport barriers [37] similar to those reported in the H-mode [38]. In the present paper, we would like to investigate the impact of probe biasing on the probe measurement itself, both fluctuations and the "macroscopic" value of the ion saturation current.

4.2 Model for the Langmuir probe, measurement of the ion saturation current

In order to model the probe in the 2D code, the parameter Λ is modified by an external control parameter, the probe biasing potential, V_{bias} . This perturbation is localized both radially and poloidally. Given the limited spacial precision of the code and the spectral treatment in the numerics, a Gaussian shape is given to V_{bias} of width $10 \times \rho_s$, Fig. 15. The electric current through the sheath is then governed by V_{bias} and the plasma response ϕ ,

$$j_{\parallel} = n(1 - \exp(\Lambda + V_{bias} - \phi)) \quad (3)$$

When $\Lambda + V_{bias} - \phi \rightarrow -\infty$, the probe works in the ion saturation current regime, the electron current is at 0. This regime is achieved with $V_{bias} \rightarrow -\infty$ and allows to measure the fluctuations of the ion saturation current in the case of fast data sampling (≥ 10 kHz). Slower acquisition rates provide the averaged ion saturation current. A standard approach for the fluctuation measurements is to neglect the fluctuations of the sound

speed, readily related to temperature fluctuations. The fluctuation of the ion saturation current is then taken as a measure of the density fluctuations. In the present model at constant temperature, this is a working assumption. It is important to stress in the presentation of the model that both ends of the flux tube are biased similarly and that the flute assumption imposes that the plasma potential ϕ remains constant along the field line. We believe that the present model of probe biasing measurement in the SOL is relevant to measurements in magnetized plasmas. However, the various assumptions that are required to allow the calculation must be kept in mind when analysing the striking results described in the following.

4.3 Perturbation of the plasma by the probe

In order to investigate the impact of probe biasing on the SOL plasma governed by the interchange turbulence discussed in this paper, we have restarted a simulation of the turbulent activity ($D = \nu = 0.01, S_0 = 0.005$), at a time well into the non-linear (saturated) regime. The control parameter V_{bias} is varied from 0 to -10 ($\Lambda = +3.878$) in 5 time steps, namely $1.710^{-2} \mu s$. This ramp time was implemented to avoid a too strong perturbation of the system. In practise, it appears that the numerics are rather robust to this perturbation. After a transient, the plasma potential settles to new profiles as exemplified on Fig. 15. It is striking to notice that the plasma potential ϕ adjusts to V_{bias} and reaches more than 75% of the biasing potential. The gaussian shape is the same as that of V_{bias} which indicates that the perturbation is smooth enough to be properly accounted for in the numerics. Away from the probe, fluctuations of ϕ around the mean value Λ are observed. As a consequence of this very strong response of the plasma potential to the probe biasing the probe is not fully operating in the saturation current regime.

Let us now consider the relaxation process of the plasma potential, Fig. 16. The characteristic time is found to be $\Omega_s t_\phi \approx 420, t_\phi \approx 1.4 \mu s$. This relaxation of the plasma potential governs the evolution of the electronic current, Fig. 17, that settles, after a transient, to 25% of the saturation current j_{sat} , so that the current to the probe is typically $0.75 j_{sat}$. This indicates that the probe in the present simulation is not biased strongly enough. Although this would be problematic in real measurements, it has a weak impact on the present analysis. Indeed, the density is directly accessible in the code. Furthermore, one can readily expect that the most important features are already captured, the increase of the biasing potential would only lead to a more pronounced effect. It is therefore our understanding that such an enhanced biasing would not change the conclusions of our work.

A clear signature of biasing is also observed on the density trace Fig. 18. When the probe biasing is switched on, one first observes a delay before the density changes. This delay of $\Omega_s t_\phi \approx 1500$ is typically the lag time for the electric potential relaxation (it is then less than 3% away from its new equilibrium value). The characteristic time for the density relaxation is found to be much longer than for the potential, typically $\Omega_s t_n \approx 3000, t_n \approx 10 \mu s$, Fig. 19. This time scale is comparable to the non-linear time for the divergence of two turbulent cases with neighbouring initial conditions, see section 3.2. It indicates that the drop in the density is governed by a complete rearrangement of the turbulent fields. Another outstanding feature of this analysis is the density decay at the probe location, Fig. 19. The density decreases by a factor 4 from 0.6 to 0.15 due to the biasing. When analysing the poloidal density profile, Fig. 20, at the probe radius, one can clearly see that the density away from the probe exhibits the same average value

and same large structures, while the density at the probe position, triangular symbol at $a\theta/\rho_s \approx 190$, is depressed. A more detailed analysis indicates that the impact of biasing is not restricted to the probe location. Indeed, the probe biasing will induce small perturbations at points that are distant from the probe. Given the exponential growth of the perturbation reported in this paper, section 3.2, one readily expects that the evolution of any point will be modified when comparing the standard simulation to that restarted with the biasing switched on. In that case, the distance between the standard simulation and the restarted simulation grows in time but the behaviour of the density field is not affected. Closer to the probe, one observes a more profound perturbation with the appearance of density fronts more frequent and regular in time.

Let us now consider the fluctuations at the probe location. The time traces are too short to provide a clean statistical analysis. However strong trends can be reported. In order to address this issue, the density and potential fluctuations have been defined by subtracting the fit of the signals, Fig. 19 and Fig. 16, from the data. The trace of these fluctuations, Fig. 21, already give a good insight into the modification of the turbulent response. For the density fluctuations, one observes the disappearance of the large events (the avalanches) and the transition to high frequency low amplitude fluctuations. The response of the electric potential fluctuations is quite different since the large amplitude fluctuations are still present, Fig. 21. On this trace, the frequency of these large bursts appears to be higher. Small scale fluctuations at high frequency also seem to be more important. Although a comprehensive statistical analysis is still required, one can conclude that the probe biasing also impacts the fluctuation measurements. Qualitatively, the large amplitude low frequency fluctuations of the density field are suppressed while the fluctuations of the electric potential appear to be shifted towards the higher frequencies. The overall effect on the transport predictions using probe fluctuation measurements is still to be determined.

5 Conclusion

Modeling of flux-driven 2D interchange turbulence in the Scrape-off Layer of fusion devices leads to a bursty transport characterized by long range transport events, sometimes called avalanches. These events are associated with radially elongated convective cells, which serve as channels for fronts of density gradient. These rare events are found to account for a significant part of the overall radial flux, in qualitative agreement with experiments, and lead to an exponential density profile. The resulting SOL e-folding length, λ_{SOL} , is found to increase very weakly with the magnitude of the driving flux. A power law dependence would yield a scaling in $S^{2/9}$. The impact of viscosity ν on turbulent transport is emphasized in this paper. Similarly to gyrokinetic simulation results, the turbulent diffusion coefficient is found to increase with ν , leading to a larger SOL width λ_{SOL} . Such a result conflicts with linear analysis, where viscosity essentially reduces the linear instability by damping small scales. It is understood as resulting from the viscous damping of sheared zonal flows, which in turn appear to control the radial correlation length of turbulence. Also discussed in this work is the modification of turbulent transport by a local biasing, possibly modeling the impact of Langmuir probe measurements. A negative biasing, resulting in the extraction of 75% of the ion saturation current, is found to strongly modify the dynamics of the transport, even outside the exact location of the biasing. At the probe top, one observes a factor 4 decrease of the time averaged

density and significant changes in the fluctuations. In particular, the large amplitude (*i.e.* strong avalanches) low frequency fluctuations of the density field are suppressed. The electric potential fluctuations exhibit essentially a shift toward larger frequencies. These results put forward the possible strong departure between Langmuir probe turbulence measurements and the "real" ambient turbulence, as well as possible mismatch in the measurement of the ion saturation current.

Acknowledgements:

The authors are pleased to thank W. Fundamenski for interesting comment. Part of this work was done during the "Festival de Théorie", Self-Organization and Transport in Electromagnetic Turbulence, Aix-en-Provence, France, July 2001.

References

- [1] G. Vayakis, AEA Fusion Report 123 (1991).
- [2] G.F. Matthews, G. Corrigan, S.K. Erents, W. Fundamenski, A. Loarte, I. Garcia-Cortes, C. Hidalgo, M.A. Pedrosa, and contributors to the EFDA-JET workprogramme, *this TCM workshop*.
- [3] J. Gunn, *Phys. of Plasmas* **8**, 1040 (2001).
- [4] R. Mitteau, Ph. Chappuis, Ph. Ghendrih, A. Grosman, D. Guilhem, J. Gunn, J. Hogan, M. Lipa, G. Martin, J. Schlosser, E. Tsitrone, *J. of Nucl. Materials* **290-293**, 1036 (2001).
- [5] X. Garbet, L. Laurent, F. Mourgues, J.P. Roubin, A. Samain, in *Proceedings of the 12th IAEA Fusion Energy Conference, Nice, 1988* (International Atomic Energy Agency, Vienna, Austria, 1989), vol. 2, p.163.
- [6] Z. Lin, T.S. Hahm, W.W. Lee, W.M. Tang, R.B. White, *Science* **281**, 1835 (1998).
- [7] Y. Sarazin, X. Garbet, Ph. Ghendrih, S. Benkadda, *Phys. of Plasmas* **7**, 1085 (2000).
- [8] S. Champeaux, P.H. Diamond, *Phys. Let. A* (2000).
- [9] P.H. Diamond, T.S. Hahm, *Phys. of Plasmas* **2**, 3640 (1995).
- [10] B.A. Carreras, D. Newman, V.E. Lynch, P.H. Diamond, *Phys. of Plasmas* **3**, 2903 (1996).
- [11] X. Garbet, R. Waltz, *Phys. of Plasmas* **5**, 2836 (1998).
- [12] P. Beyer, S. Benkadda, X. Garbet, P.H. Diamond, *Phys. Rev. Let.* **85**, 4892 (2000).
- [13] A. Thyagaraja, *Plasma Phys. Control. Fusion* **42**, B255 (2000).
- [14] Y. Sarazin, Ph. Ghendrih, *Phys. of Plasmas* **5**, 4214 (1998).
- [15] P.A. Politzer, *Phys. Rev. Let.* **84**, 1192 (2000).

- [16] Ch.P. Ritz, R.V. Bravenec, P.M. Schoch, R.D. Bengtson, J.A. Boedo, J.C. Forster, K.W. Gentle, Y. He, R.L. Hickok, Y.J. Kim, H. Lin, P.E. Philips, T.L. Rhodes, W.L. Rowan, P.M. Valanju, A.J. Wootton, *Phys. Rev. Let.* **62**, 1844 (1989).
- [17] A.V. Nedospasov, *Sov. J. Plasma Phys.* **15**, 659 (1989).
- [18] X. Garbet, L. Laurent, J.-P. Roubin, A. Samain, *Nucl. Fusion* **31**, 967 (1991).
- [19] M. Endler, H. Niedermeyer, L. Giannone, E. Holzhauer, A. Rudyj, G. Theimer, N. Tsois, ASDEX team, *Nucl. Fusion* **35**, 1307 (1995).
- [20] S. Benkadda, X. Garbet, A. Verga, *Contrib. Plasma Phys.* **34**, 247 (1994).
- [21] C. Hidalgo, M.A. Pedrosa, B. van Milligen, E. Sanchez, R. Balbin, I. Garcia-Cortes, J. Bleuel, L. Giannone, H. Niedermeyer, *Fusion Energy 1996 (Proc. 16th Int. Conf. Montreal, 1996)*, Vol. 1, IAEA, Vienna 617 (1997).
- [22] G.Y. Antar, P. Devynck, X. Garbet, S.C. Luckhardt, *Phys. of Plasmas* **8**, 1612 (2001).
- [23] B.A. Carreras, C. Hidalgo, E. Sánchez, M.A. Pedrosa, R. Balbin, I. Garcia-Cortés, B. van Milligen, D.E. Newman, V.E. Lynch, *Phys. of Plasmas* **3**, 2664 (1996).
- [24] Z. Lin, T.S. Hahm, W.W. Lee, W.M. Tang, P.H. Diamond, *Phys. Rev. Let.* **83**, 3645 (1999).
- [25] P.H. Diamond, M.N. Rosenbluth, F.L. Hinton, M. Malkov, J. Fleischer, A. Smolyakov, in *Proceedings of the 17th IAEA Fusion Energy Conference, Yokohama, 1998* (International Atomic Energy Agency, Vienna, Austria, 1999), vol. 4, p. 1421.
- [26] L. Chen, Z. Lin, R. White, *Phys. of Plasmas* **7**, 3129 (2000).
- [27] S. Coda, M. Porkolab, K.H. Burrell, *Phys. Rev. Let.* **86**, 4835 (2001).
- [28] R.A. Moyer, G.R. Tynan, C. Holland, M.J. Burin, *Phys. Rev. Let.* (2001), in press.
- [29] T.S. Hahm, M.A. Beer, Z. Lin, G.W. Hammet, W.W. Lee, W.M. Tang, *Phys. of Plasmas* **6**, 922 (1999).
- [30] M.N. Rosenbluth, F.L. Hinton, *Phys. Rev. Let.* **80**, 724 (1998).
- [31] B.N. Rogers, W. Dorland, M. Kotschenreuther, *Phys. Rev. Let.* **85**, 5336 (2000).
- [32] A.M. Dimits, T.J. Williams, J.A. Byers, B.I. Cohen, *Phys. Rev. Let.* **77**, 71 (1996).
- [33] M.A. Malkov, P.H. Diamond, to appear in *Phys. of Plasmas* (2001).
- [34] L. Tonks, I. Langmuir, *Phys. Review* **34**, 876 (1929).
- [35] P.C. Stangeby, M.C. McCracken, *Nucl. Fusion* **30**, 1225 (1990).
- [36] B. Richards, T. Uckan, A.J. Wootton, B.A. Carreras, R.D. Bengtson, P. Hurwitz, G.X. Li, H. Lin, W.L. Rowan, H.Y.W. Tsui, A.K. Sen, J. Uglum, *Phys. of Plasmas* **1**, 1606 (1994).
- [37] R.R. Weynants, G. van Oost, G. Bertschinger *et al.*, *Nucl. Fusion* **32**, 837 (1992).
- [38] The ASDEX team, *Nucl. Fusion* **29**, 1959 (1989).

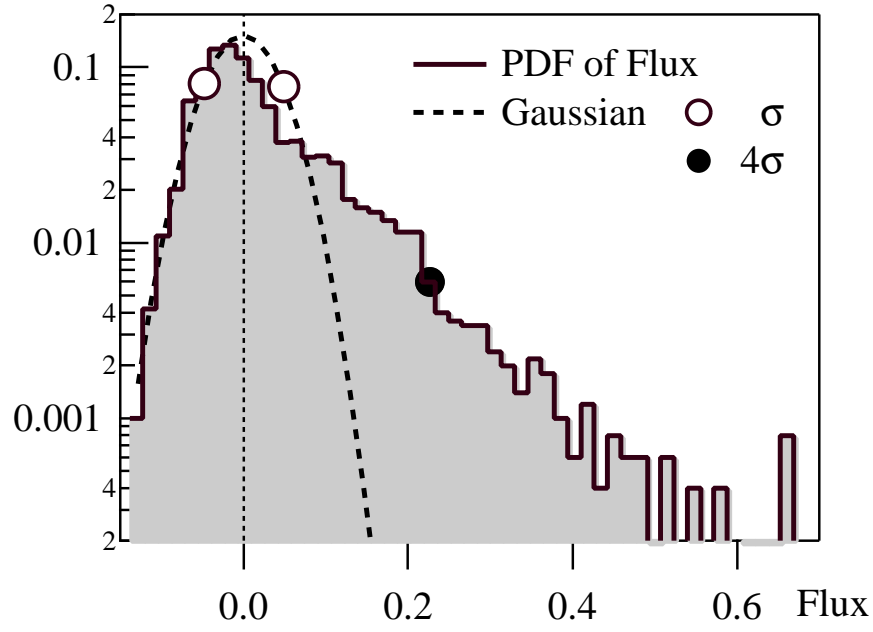


Figure 1: Probability Density Function of the turbulent radial flux. A gaussian of vanishing mean flux fits the PDF of the inward flux (negative values).

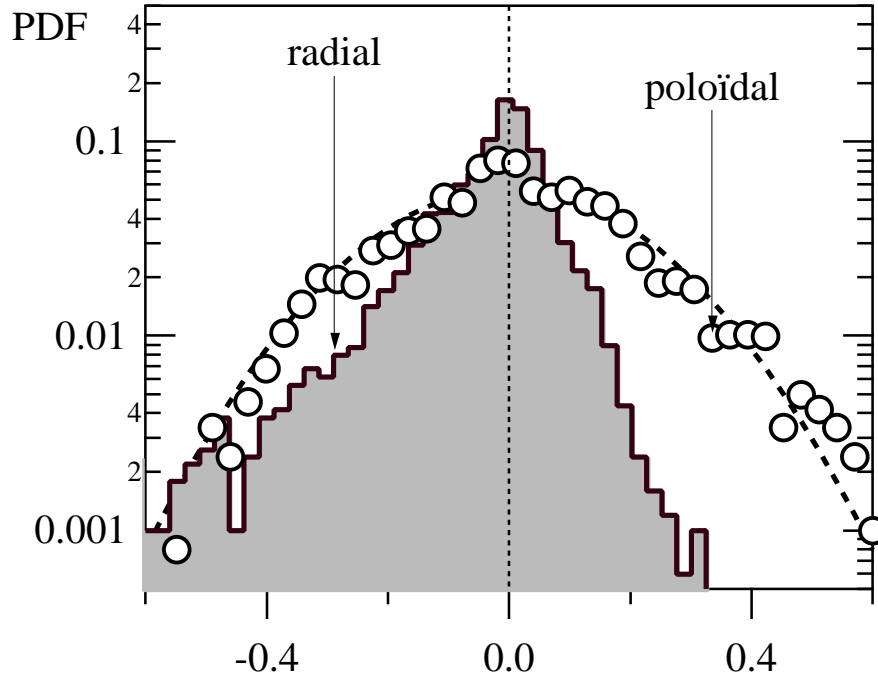


Figure 2: Probability Density Function of the radial and poloidal density gradients. Poloidal gradient exhibits an almost gaussian PDF.

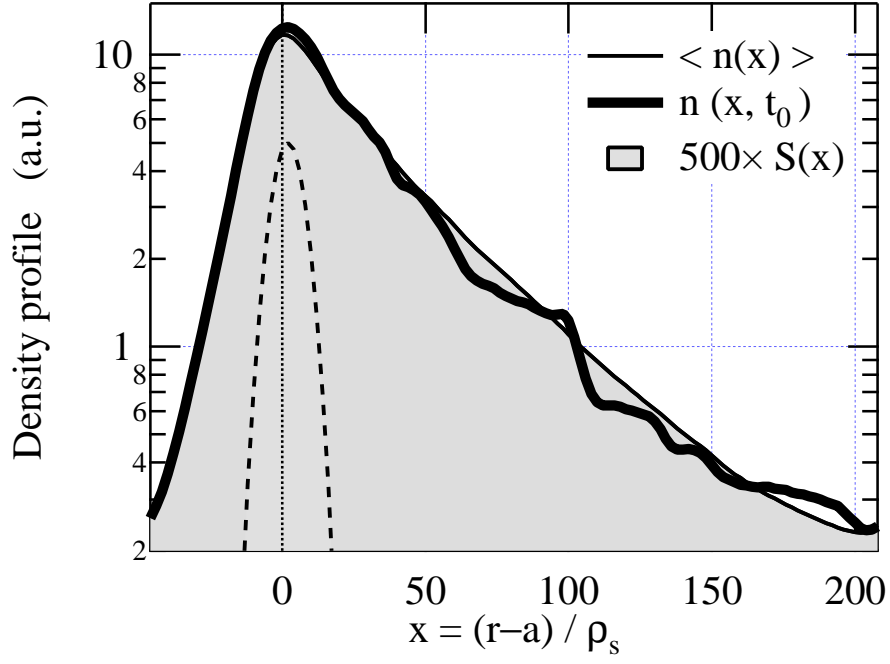


Figure 3: Time averaged and instantaneous density profiles (case $\nu_0 = 5.10^{-3}$). The source is magnified 500 times.

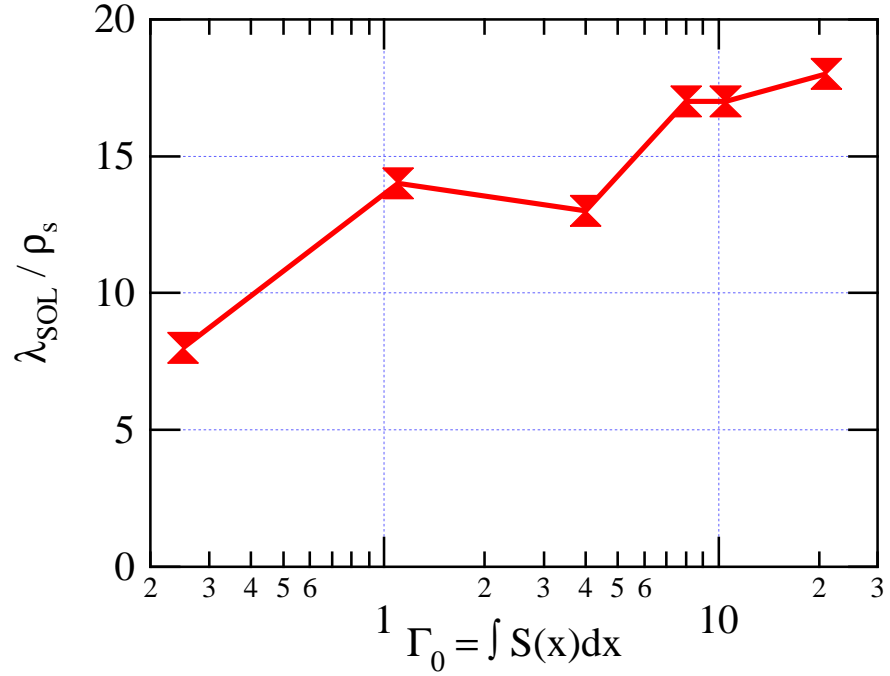


Figure 4: Increase of SOL e-folding length λ_{SOL} with the driving flux $\Gamma_0 \doteq \int_0^{L_x} S(x) dx$. These simulations have been performed with the following set of normalized parameters: $g = 5.10^{-4}$, $\sigma_{||} = 10^{-5}$, $D = \nu = 5.10^{-4}$. The grid size is equal to 64×64 .

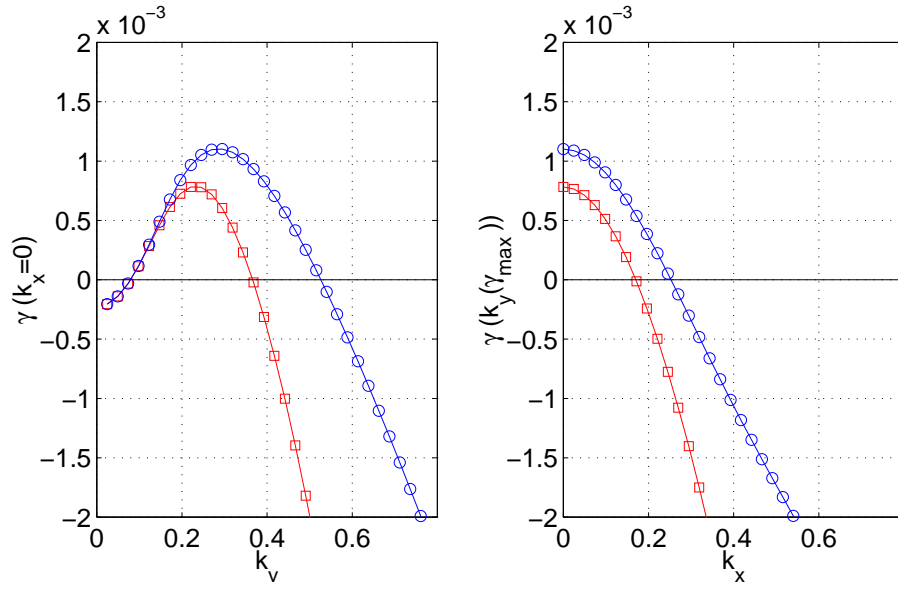


Figure 5: Normalised linear growth rate for two values of the viscosity. $k_y(\gamma_{max} \approx 11.10^{-4}) \approx 0.29$ for $\nu_0 = 5.10^{-3}$ (circles) and $k_y(\gamma_{max} \approx 7.810^{-4}) \approx 0.22$ for $\nu_1 = 2.10^{-2}$ (squares).

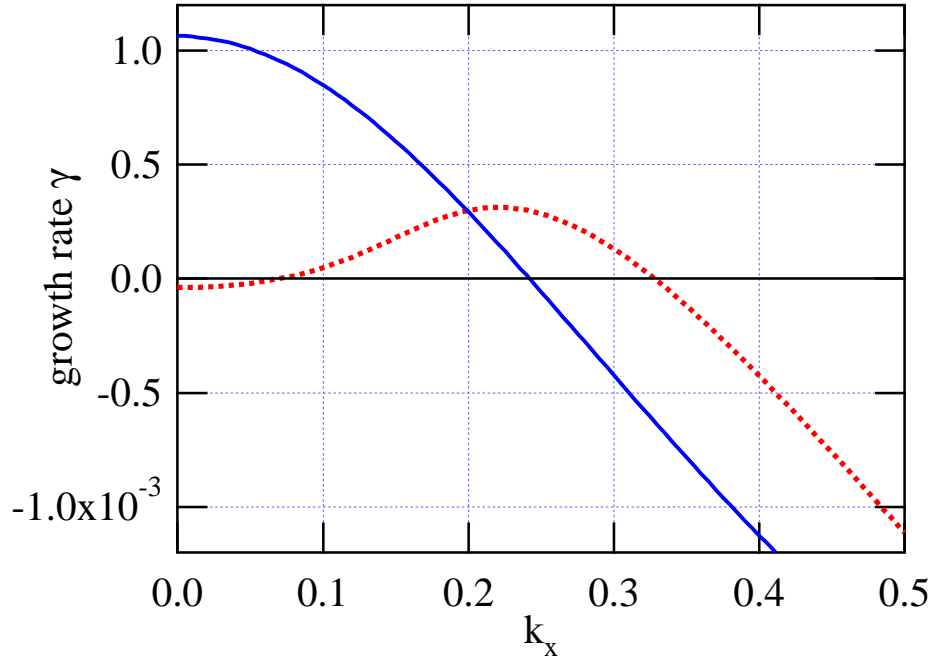


Figure 6: Linear growth rate computed at $k_y = 0.25$ with $(\sigma_{||}; \bar{v}'') = (2.310^{-4}; 0)$ (solid) and $(\sigma_{||}; \bar{v}'') = (0; 2.310^{-3})$ (dashed). All other parameters are defined in text. \bar{v}'' appears to introduce a linear characteristic radial scale of the fluctuations.

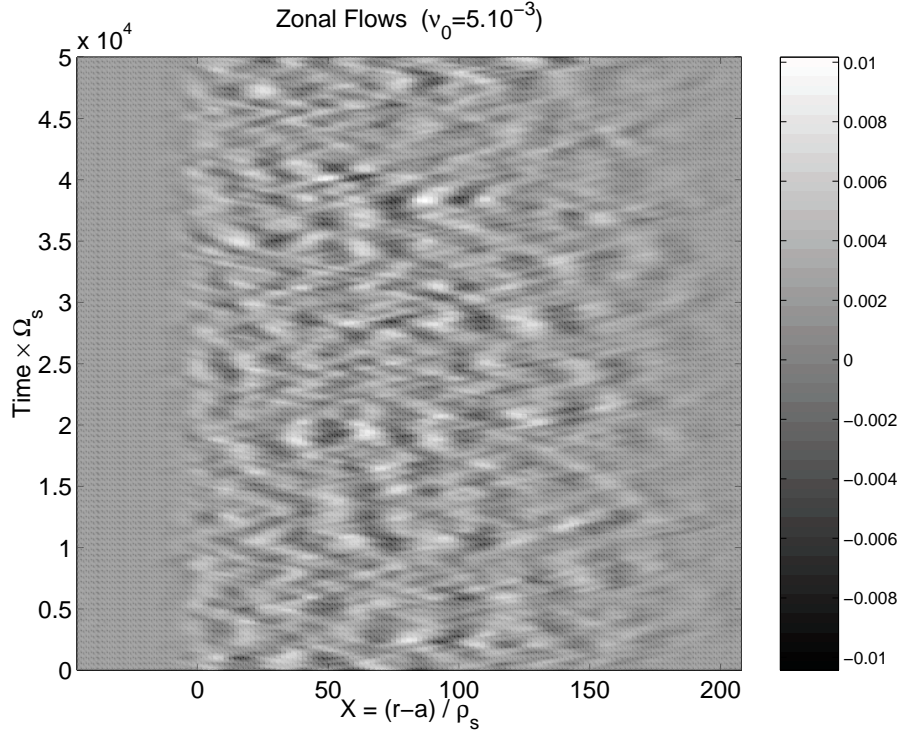


Figure 7: Time evolution of \bar{v}_y for $\nu_0 = 5.10^{-3}$.

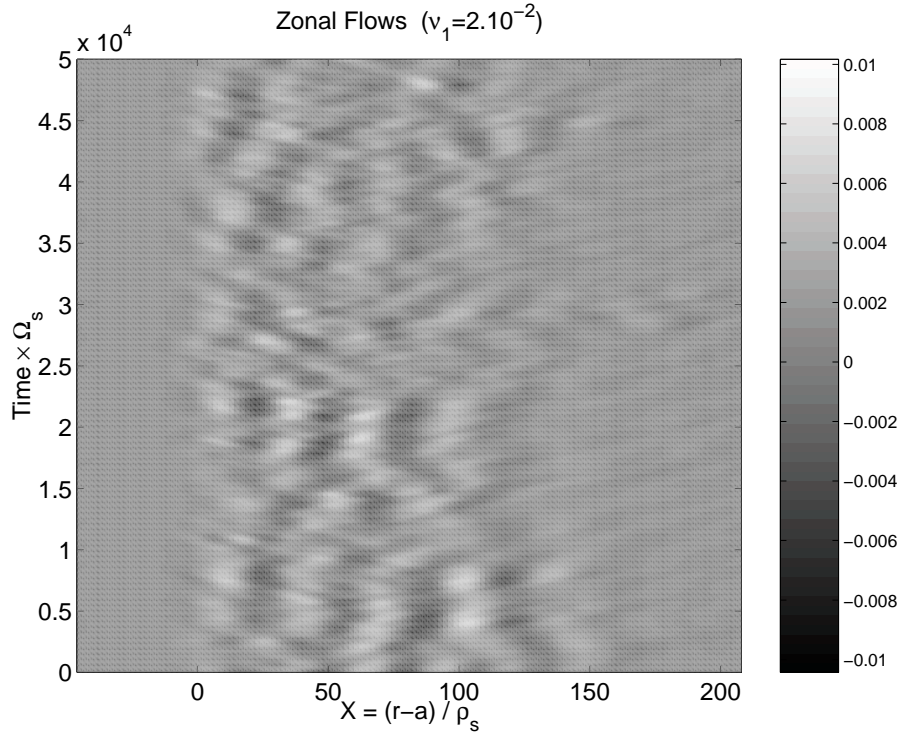


Figure 8: Time evolution of \bar{v}_y for $\nu_1 = 2.10^{-2}$.

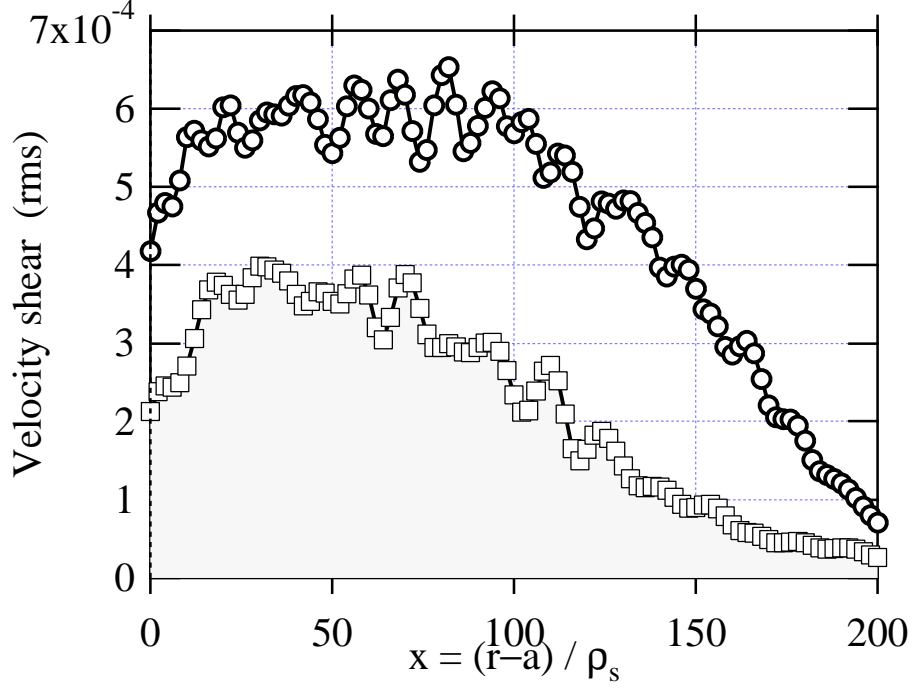


Figure 9: Root mean square of velocity shear $\langle(\partial_x \bar{v})^2\rangle^{1/2}$ for $\nu_0 = 5.10^{-3}$ (circles) and $\nu_1 = 2.10^{-2}$ (squares).

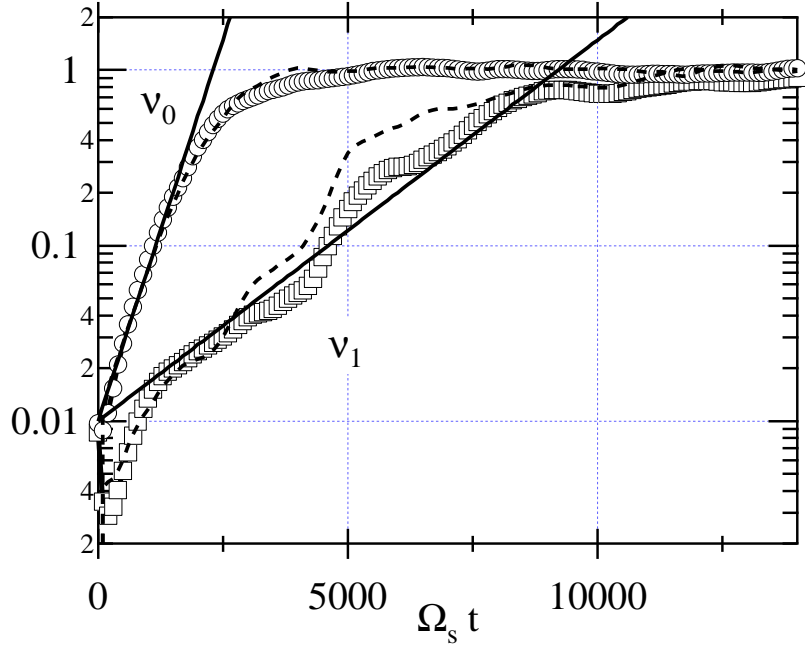


Figure 10: Divergence of two simulations whose potential differs initially by a white noise of relative magnitude equal to 10^{-2} . Divergence of potential is quantified by $\langle(\tilde{\phi}_{WN} - \tilde{\phi})^2\rangle^{1/2} / \langle\tilde{\phi}_{WN}^2 + \tilde{\phi}^2\rangle^{1/2}$, where $\langle...\rangle$ refers to $\iint ... dx dy$. Dashed lines refer to divergence of density. Divergence looks exponential, with $\gamma \approx 2.10^{-3}$ for $\nu_0 = 5.10^{-3}$ (circles) and $\gamma \approx 5.10^{-4}$ for $\nu_1 = 2.10^{-2}$ (squares).

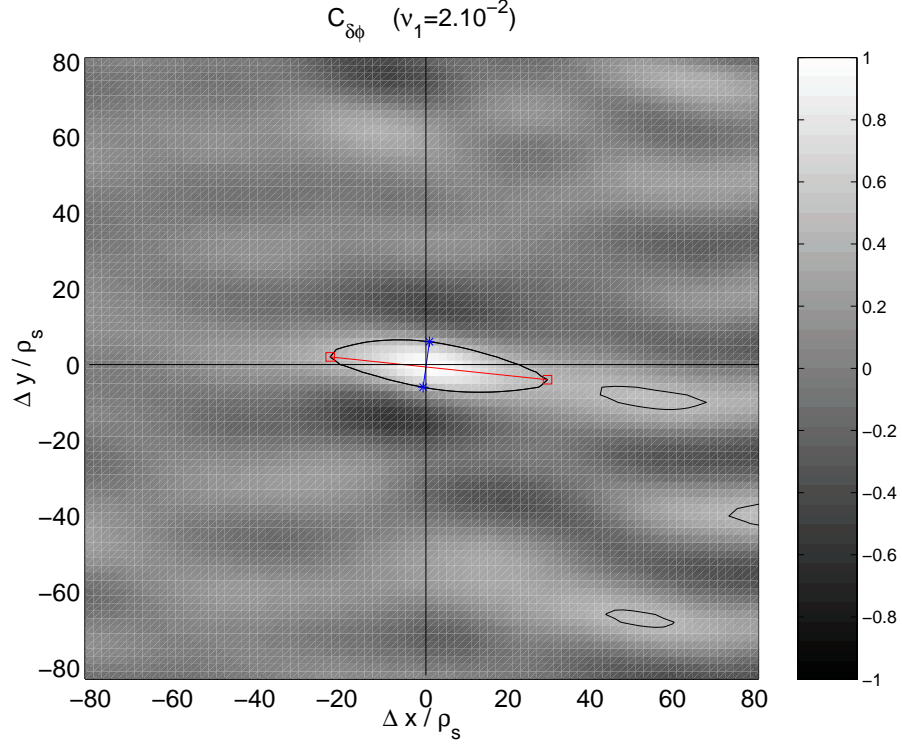


Figure 11: Self-correlation function $C_{\tilde{\phi}}(\Delta x, \Delta y)$ of $\tilde{\phi}$ at time $t \approx 11.5\mu s$ for $\nu_1 = 2.10^{-2}$. The two lines centered on $(\Delta x, \Delta y) = (0, 0)$ correspond to λ_{correl} and λ_{\perp} (see text).

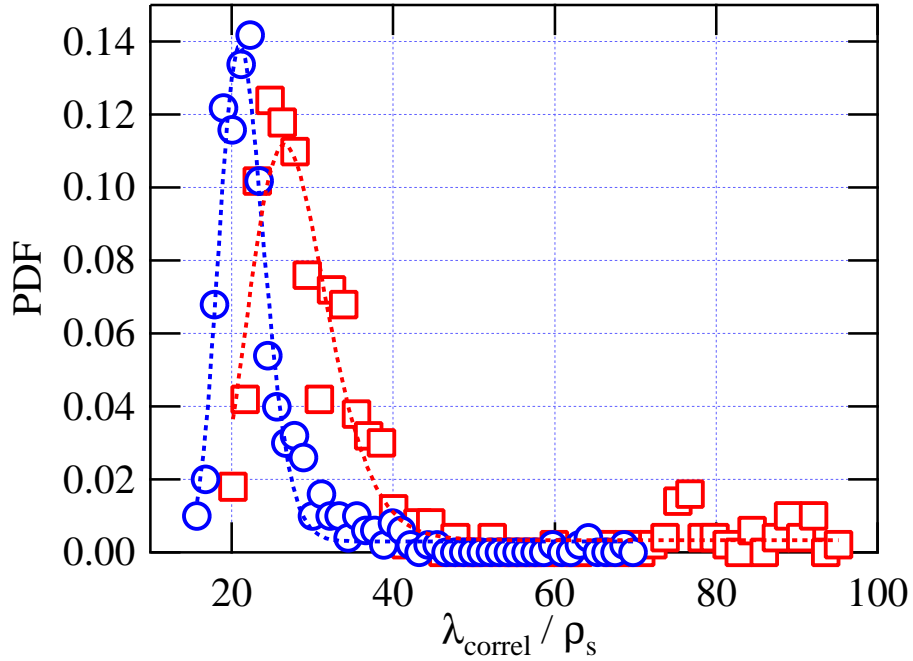
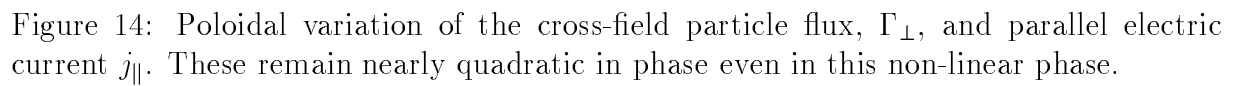
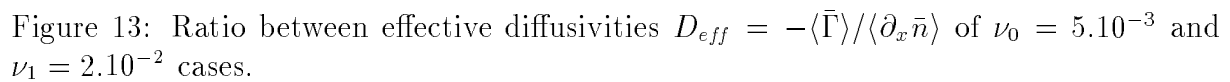


Figure 12: PDF of the correlation length λ_{correl} , as defined in the text, for $\nu_0 = 5.10^{-3}$ (circles) and $\nu_1 = 2.10^{-2}$ (squares). Dashed lines are Log-normal distributions plotted "to guide the eyes".



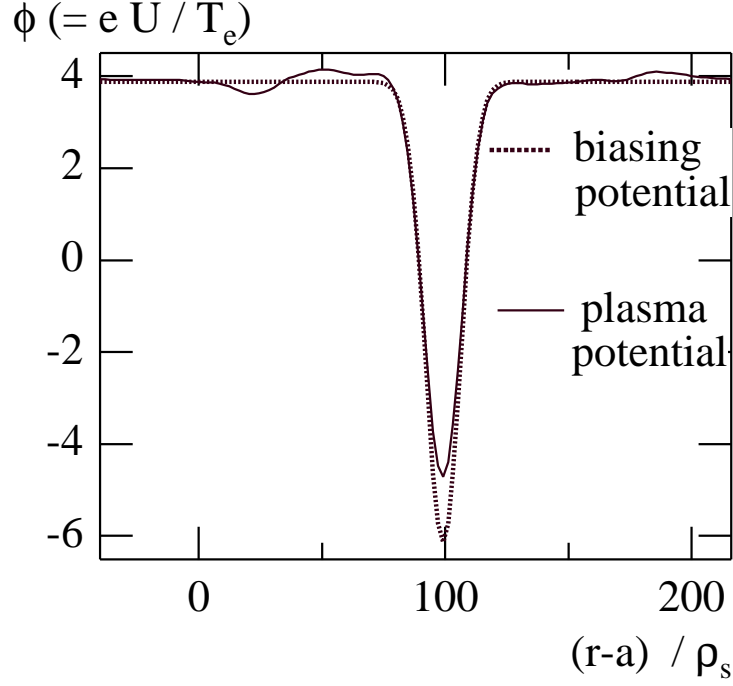


Figure 15: Radial profile of the floating potential and of the externally applied electric potential. The probe is localized at $(r - a)/\rho_s \approx 100$. In this model, the probe is quite massive, typically $10 \rho_s$. The plasma potential accounts for most of the externally imposed electrostatic potential.

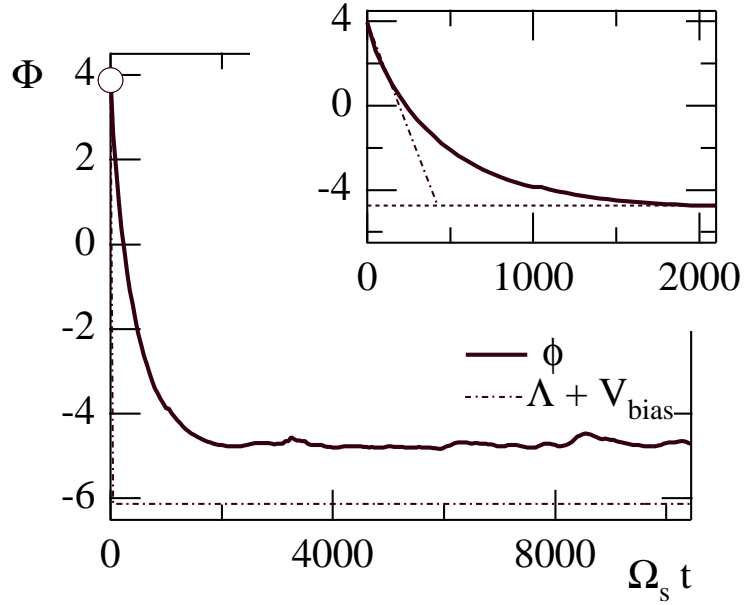


Figure 16: Evolution of the plasma potential at the probe (plain line) in response to the probe biasing (dash-dot line). Blow-up, characteristic time of this relaxation $\Omega_s t \approx 423$.

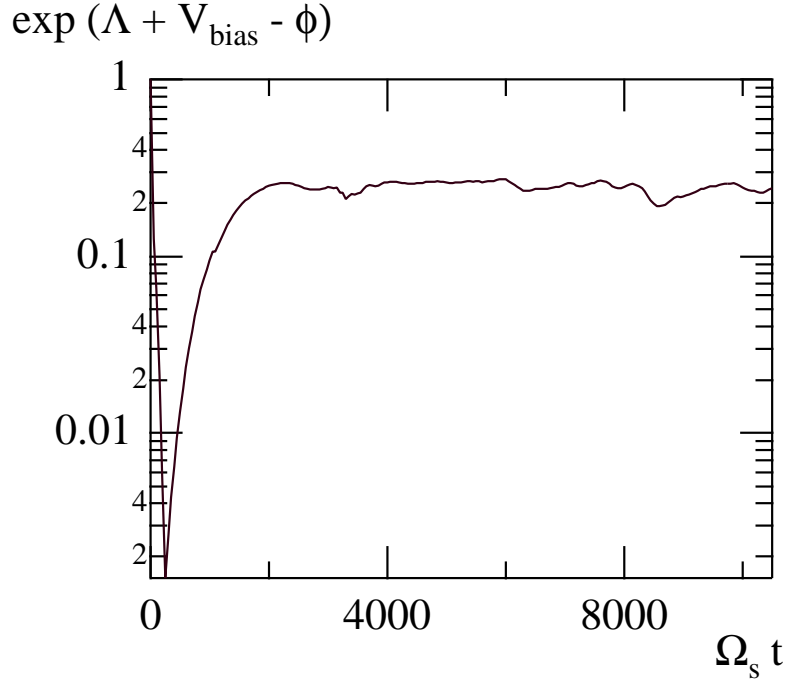


Figure 17: Evolution of the electronic current at the probe, after a sharp decrease to zero the electronic current settles at 25% of the saturation current. The characteristic time of this relaxation is that of the plasma potential, $\Omega_s t \approx 423$.

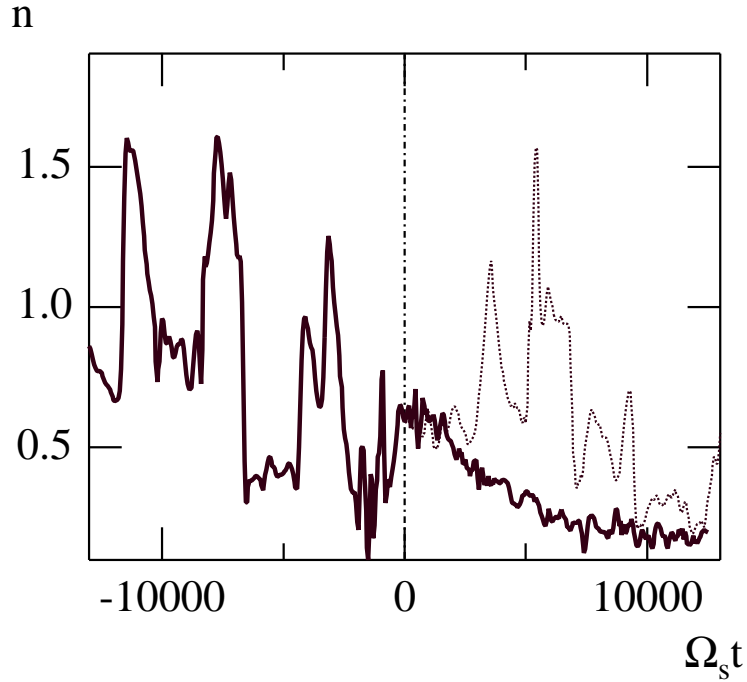


Figure 18: Evolution of the density at the probe, before biasing with $\Omega_s t < 0$ and after biasing with $\Omega_s t > 0$ (plain curve). The fluctuations are significantly reduced with biasing and a relaxation of the mean density is observed. The dashed curve is the output from the simulation with no biasing all along the simulation.

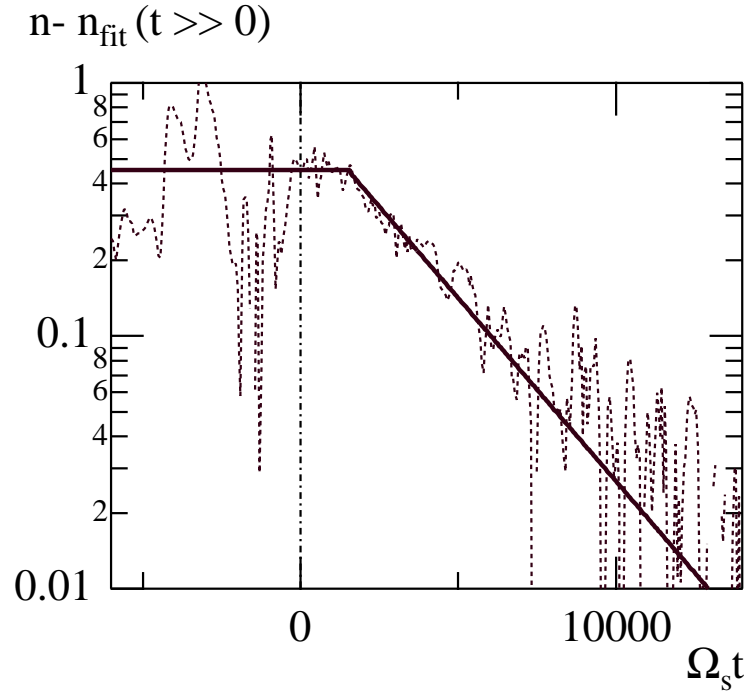


Figure 19: Evolution of the density at the probe, before biasing with $\Omega_s t < 0$ and after biasing with $\Omega_s t > 0$. After subtracting the equilibrium density with biasing, $n_{\text{fit}}(t \gg 0) \approx 0.1485$, one finds a good exponential fit for the density decay.

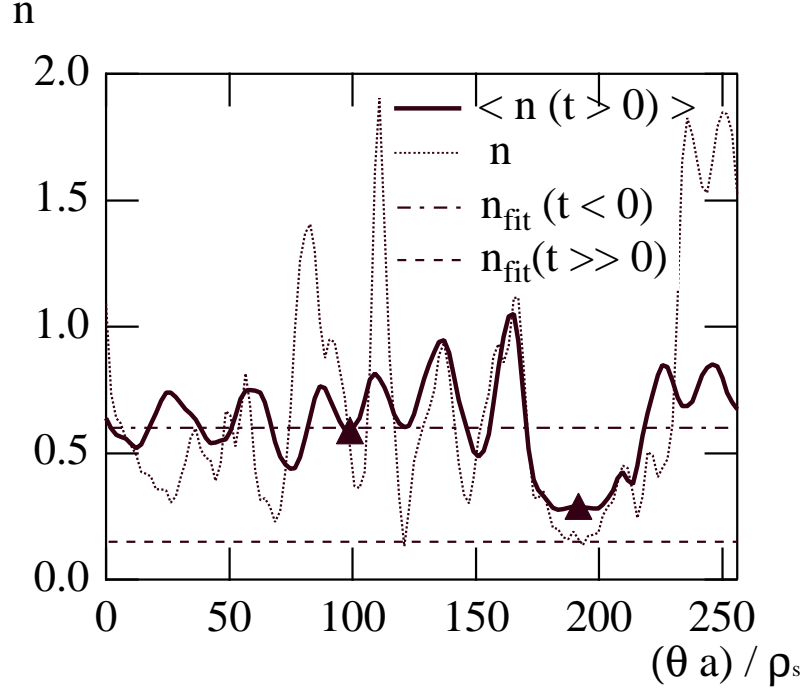


Figure 20: Profile of the density in the poloidal direction at the probe radial position, with the time averaged profile, the density at a given time as well as the location of the probe at $a\theta/\rho_s \approx 190$ and a reference point at $a\theta/\rho_s \approx 100$. The time average includes a significant part of the relaxation so that the average value plotted here is larger than the steady state value.

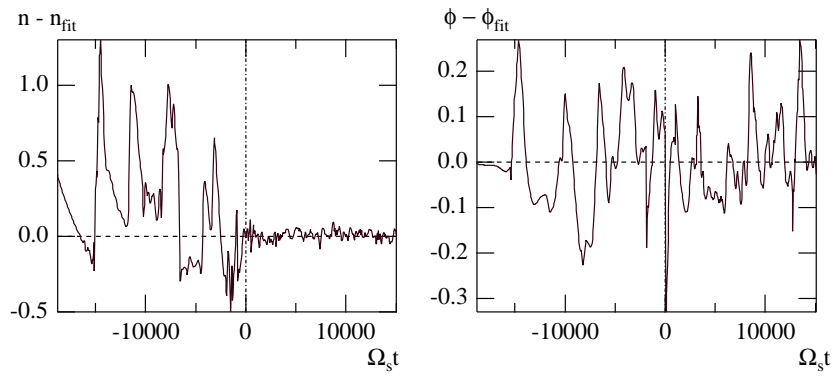


Figure 21: Traces of the density and electric potential fluctuations at the probe. The fluctuation data is obtained by subtracting the fit of the relaxation Fig. 19 and of the electric potential. As in previous graphs, time zero marks the beginning of the probe biasing.